



BIOMATERIALS

Sensorimotor control of robots mediated by electrophysiological measurements of fungal mycelia

Anand Kumar Mishra¹, Jaeseok Kim², Hannah Baghdadi¹, Bruce R. Johnson³, Kathie T. Hodge⁴, Robert F. Shepherd^{1*}

Copyright © 2024 the Authors, some rights reserved; exclusive licensee American Association for the Advancement of Science. No claim to original U.S. Government Works

Living tissues are still far from being used as practical components in biohybrid robots because of limitations in life span, sensitivity to environmental factors, and stringent culture procedures. Here, we introduce fungal mycelia as an easy-to-use and robust living component in biohybrid robots. We constructed two biohybrid robots that use the electrophysiological activity of living mycelia to control their artificial actuators. The mycelia sense their environment and issue action potential–like spiking voltages as control signals to the motors and valves of the robots that we designed and built. The paper highlights two key innovations: first, a vibration- and electromagnetic interference–shielded mycelium electrical interface that allows for stable, long-term electrophysiological bioelectric recordings during untethered, mobile operation; second, a control architecture for robots inspired by neural central pattern generators, incorporating rhythmic patterns of positive and negative spikes from the living mycelia. We used these signals to control a walking soft robot as well as a wheeled hard one. We also demonstrated the use of mycelia to respond to environmental cues by using ultraviolet light stimulation to augment the robots' gaits.

INTRODUCTION

With extreme care and effort, robots can operate with animal-like gaits that impress even a lay audience. The efficiency, durability, repeatability, and capabilities of these demonstrations, however, still do not match those of their biological counterparts, such as dogs and humans.

Organisms solve these hardware issues by growing, not assembling, sensors, actuators, and the neural networks that connect them. A human fingertip, for example, has more than 3000 mechanoreceptors attached to thousands of interconnected nerves and neuronal signaling pathways that communicate with a distally located brain (1, 2). The nanoscale bottom-up assembly processes that enable these features are not a capability of human technology yet; therefore, synthetic robots do not approach the capabilities of natural organisms. One approach for biohybrid robots is the use of living tissue to control mechanisms (3, 4). In some ways, this approach is akin to the use of unconventional computing to control robots (5) as opposed to traditional controllers, such as the design of Belousov-Zhabotinsky liquid marbles with light-stimulated controllers, chemical taxis controllers (6–9), and autonomous liquid robots (10).

Two primary methods of living biohybrid machine construction involve directing cultured cells into useful forms and excising and using tissues after natural formation. Among the five kingdoms, animal-based biohybrid machines are the most popular in literature because of their implied motility (11, 12), and, after forming the tissue construct, they have been controlled by pulses of optical, electrical, or magnetic stimuli (11, 13).

Culturing animal cells typically involves growing muscle bundles from single cells through self-assembly and embedding them into mechanical structures or scaffolding (11, 13). This method has

been applied to various biohybrid robots usually composed of either skeletal or cardiac muscle cells (3, 14–21). Whole muscle tissues have also been used for biohybrid robots, where their actuation is typically triggered electrically or chemically (4, 22–26). Animal biohybrids have been used for swimming, walking, and other behaviors—for example, frog and cardiac muscles for swimming (22, 23), *Aplysia californica* I2 muscles for walking (24), earthworm muscles for bio-micropumps and valves (4, 25), and neural cells to control robots (27). Although these accomplishments are exciting, there are many challenges to solve related to animal biohybrids and the difficulty of maintaining healthy, living tissues in pragmatic environmental conditions (28). For example, a sterile environment and daily medium exchange with infusion of supplements and antibiotics such as penicillin are required to maintain living cell cultures.

Nonanimal systems have started to garner interest because they may be less prone to some of these issues and provide other opportunities, such as reduced complexity. These nonanimal biohybrids are primarily based on plants and bacteria. Like animals, bacteria are predominantly researched because of their motility (12) and have been used for tumor site detection (29), targeted payload delivery (30), and micromotors (31). Plant-based biohybrid systems are typically built not only for nontraditional robotics use cases, such as environmental sensing (32) and energy harvesting (33), but also as actuators (34). The relatively short life span of individual bacteria and a plant's slower movements [see exceptions (35, 36)] provide challenges. Slime mold (*Physarum polycephalum*) has also been used to control robots through its physical oscillatory movements (37), but the shape change is on the order of minutes.

The kingdom Fungi is less explored for biohybrid robots; however, it offers several potential advantages over other kinds of organisms. Unlike animal cells, fungi can be easily cultured in large quantities and have relatively simple engineering requirements for sustaining life (38, 39). Common fungal species have demonstrated the ability to thrive in extreme environments, including the Arctic and Antarctic (40), nuclear radiation sites (40, 41), and highly acidic or saline conditions (42), making them promising candidates for

¹Sibley School of Mechanical and Aerospace Engineering, Cornell University, Ithaca, NY 14853, USA. ²Department of Industrial Engineering, University of Florence, Florence, Tuscany 50139, Italy. ³Department of Neurobiology and Behavior, Cornell University, Ithaca, NY 14853, USA. ⁴Plant Pathology and Plant-Microbe Biology Section, School of Integrative Plant Science, Cornell University, Ithaca, NY 14853, USA. *Corresponding author. Email: rfs247@cornell.edu

various robotics applications requiring robust operation in hazardous conditions.

Mycelial networks comprise the mostly subterranean portion of fungi; they sense, communicate, and transport nutrients and water (43). Mycelia are composed of filamentous, branching hyphae and can grow to extremely large scales (44). Their interconnected, complex networks exhibit rapid signal transmission, growth, and the production of signaling molecules (38, 45, 46).

These fungi are also sensitive to environmental cues, such as light and chemicals (39). Their light sensitivity is believed to be because of proteins, such as opsins, phytochromes, and white collar-1 (WC-1), that change conformation in response to light. WC-1 is a blue-light photoreceptor that is sensitive to the wavelengths between blue and ultraviolet (UV) (39, 47, 48). These light-sensitive proteins are also likely involved in hyphal growth regulation and circadian rhythms (49).

The electrical signals that are indicative of these environmental cues, as well as other regulatory processes, are transmitted through the transmembrane movement of ions. Action potential-like signals have been recorded intracellularly and extracellularly from several fungal species, such as *Neurospora crassa* (45), *Armillaria bulbosa* (46), *Ganoderma resinaceum* (50), and *Pleurotus djamor* (51). For example, *A. bulbosa* can produce electrical signals between 1 and 5 Hz under mechanical stimulation (46). Mechanically sensitive ion channels permeable to calcium and potassium have been described in fungal species (52). Changes in membrane potential producing action potential-like events may be mechanistically similar to the depolarization and repolarization phases of action potentials in animal neurons (53). Our intention in this work was not to explore the mechanisms of electrical excitability in fungi but, instead, to use these signals to sense the environment and control robots.

Fungi have recently drawn the attention of researchers who are interested in harnessing their unique characteristics to develop biohybrid solutions. Some examples where a living fungus was used for biohybrid applications include pressure-detection insoles (54), fungal “skin” sensors (55), self-healing mycelium-based composite materials created using 3D-printed hydrogel matrices (56), and the mapping of action potential waveforms to 50 different English words (57).

Here, we introduce biohybrid robots controlled by fungal mycelia, focusing on two key advancements. First, we have developed a vibration- and electromagnetic interference (EMI)-shielded mycelium-electrical interface for stable, long-term bioelectric recordings during untethered, mobile operation. Second, we have crafted a control architecture for robots inspired by neural central pattern generators, incorporating rhythmic patterns of positive and negative spikes from living mycelia. We combined these two advances to use mycelia to control the locomotion of both a tethered, 3D-printed soft robot and an untethered, wheeled robot. In both cases, we also demonstrated the use of UV light incident on the mycelia to alter the trajectories of the robots.

RESULTS

Fungal mycelium

We selected *Pleurotus eryngii* as the fungus to interface with our electromechanical system because of its favorable characteristics, such as filamentous mycelial growth pattern, rapid growth rate, and nonpoisonous character (58). Our fungal culture protocol used the following steps: agar medium preparation and sterilization, transfer

of the medium to petri dishes, inoculation, incubation, and subculturing (see fig. S1, steps 1 to 7). We conducted mycelium growth tests in petri dishes of two sizes: small (60 mm) and large (150 mm) diameters. The fungus typically requires ~ 14 to 33 days to fully integrate into the robot's scaffolding, depending on the dish size. Detailed methodologies and results can be found in Fig. 1A, fig. S2 (A and B), the Fungal culture protocols section, and the Growth test section in the Supplementary Methods.

Hardware design for stable electrophysiological mycelium measurement

We chose extracellular electrophysiology (EEP) methods to establish a bioelectric connection between *Pleurotus* mycelia and our robot's microcontroller unit (MCU). EEP offers several advantages, including noninvasiveness, wide spatial contact with mycelia, stable long-term recordings, and high temporal resolution when using differential electrodes (59, 60).

We used this mycelium scaffold to measure voltage spikes from the hyphal bundles, as shown in Fig. 1A. The plates featured three electrode inputs (E_1 , E_2 , and E_{GND} ; Fig. 1B). Figure 1C displays the scaffold integrated with its casing, electrodes, and mycelia. We also demonstrated effective electrode positioning, allowing the mycelia to grow onto the electrodes and ensuring stable and cohesive contact with the hyphal bundles. Several microscopic images capturing these interfaces and the fungal mycelia are presented in Fig. 1D and fig. S3 (A to D). Detailed discussions on the fabrication and integration procedures of the 3D-printed scaffold, along with the imaging procedure, are described in the 3D-printed mycelium scaffold section and the Fungi imaging section in the Supplementary Methods. These scaffold modules facilitated the growth of the mycelia into the electromechanical robot interface; for instance, a starfish-like legged soft robot is illustrated in Fig. 1E. The mycelia within the scaffold generate spontaneous electrical action potential-like signals and are also capable of producing these potentials in response to UV stimulation. These signals function as both motor commands and sensory feedback, allowing the robot to control its movement. The techniques that we use to measure these signals have been used previously for other biological cells and tissues (59, 60). The bioelectric, possibly cellular-level circuit model that we use is based on Ohm's law and is depicted in Fig. 2A

$$V_{\text{native}} = I_m Z_e \quad (1)$$

where V_{native} is the spontaneous action potentials, I_m is the membrane current, and Z_e is the equivalent impedance.

In addition, for the signal recording circuit, we used two electrodes (E_1 and E_2) in the mycelium and a ground electrode (E_{GND}) in agar medium. We connected E_1 and E_2 to differential input ports and E_{GND} to a ground port of our high-resolution data acquisition system (ADC-24, PicoLog) that has a 24-bit analog-to-digital converter (ADC) with four channels and a maximum sampling rate of 16 S s^{-1} . We placed the measurement setup in a custom-built Faraday cage for long-term recordings. The complete measurement setup is shown in Fig. 2B and fig. S4 (A and B), and setup requirements and fabrication are thoroughly discussed in the Fungal signal recording setup section.

Signal acquisition

We measured bioelectrical signals from fungi in several small (60 mm, fig. S5A) and large (150 mm, fig. S5B) plates inoculated with

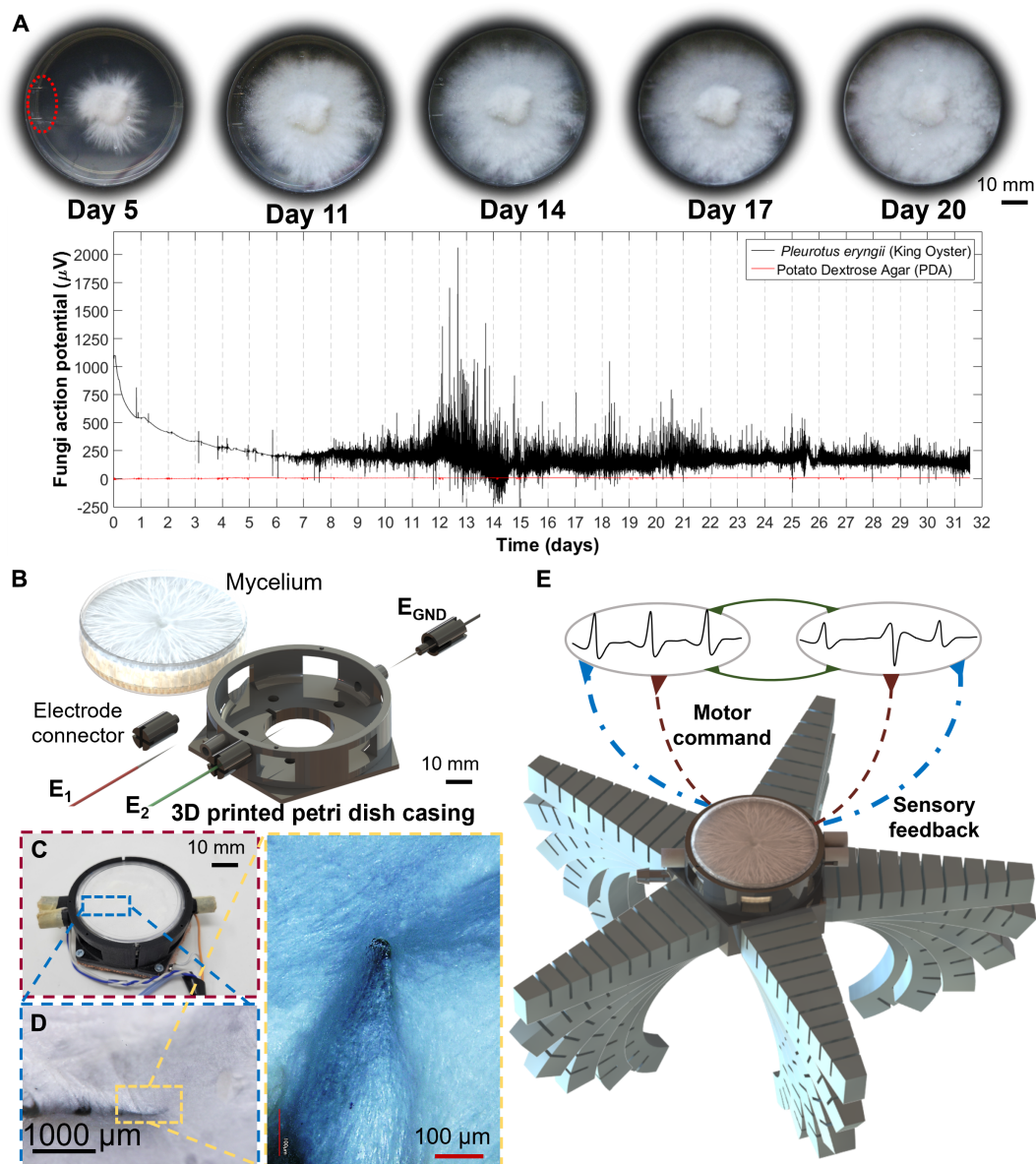


Fig. 1. Fungal bioelectric signal recording and robot interface. (A) Mycelium growth and electrical signal recording were conducted over a 4-week period on small plates, with no electrical events observed in the control plate (only PDA). A red dotted circle highlights both electrodes. (B) Depiction of 3D-printed scaffold design with mycelia and electrodes. (C) Fabricated scaffold. (D) Microscopic imaging of the mycelium-electrode interface at two magnifications. (E) Starfish-like soft robot design and working principle.

mycelia over a period of more than 30 days. To validate the authenticity of the signals, we used a pure agar plate as a control. Our recording procedure involved recording from the day of inoculation, as the mycelia grew and visually reached the electrodes on the small plate, and recording from a fully grown mycelium plate, with a parallel agar plate serving as a control for comparison. We have presented the bioelectric signals from both the plates and the control in Fig. 1A and fig. S5C. Before starting the electrical recordings, we also measured the electrode dc resistance in both the mycelium-grown and control plates. The electrode resistance was 2.2 ± 0.2 megohms for the agar plate and 1.4 ± 0.25 megohms for the mycelium plate.

Our recorded data display no electrical spiking activity before the hyphae contacting the electrodes or in control plates with a baseline signal of $<20 \mu\text{V}$ (refer to Fig. 1A and fig. S5C). Conversely, we observed large spiking activity in mycelium plates. We discussed resistance, bioelectric signals, and signal authenticity measurement procedures in the Electrode resistance and Mycelium scaffold signal recording setup sections in the Supplementary Methods.

Signal processing and analysis

We processed the raw signals from the 30-day-long recorded fungal datasets by considering several factors: baseline voltage, sampling, digital filtering, noise exclusion, data normalization, prominent

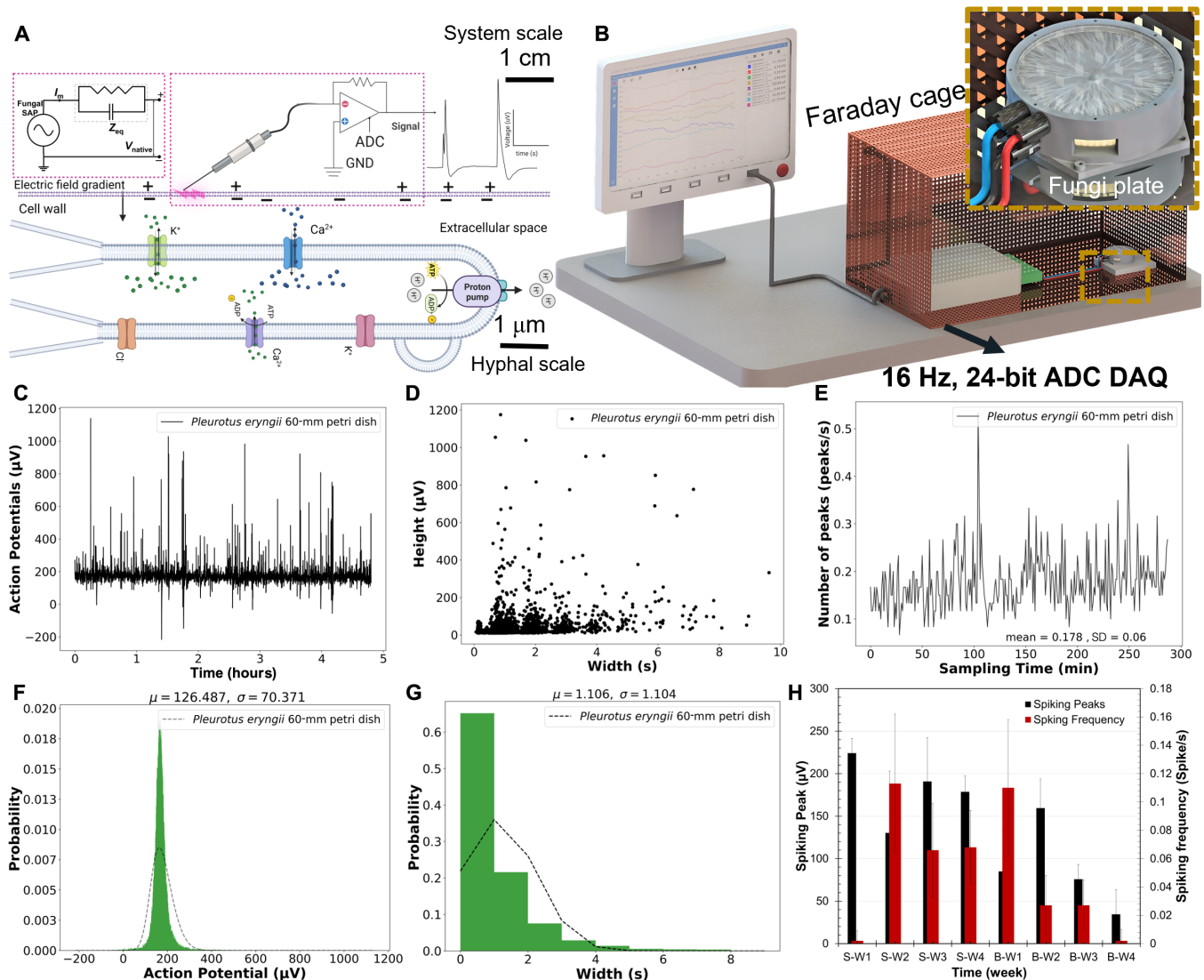


Fig. 2. Fungal electrical recording preparation and signal analysis. (A) Bioelectric circuit diagram of electrode connection with mycelial membrane through EEP. (B) The signal measurement setup involves a scaffold with electrodes connected to a high-resolution, 24-bit analog-to-digital DAQ system (PicoLog). The entire setup is housed inside a Faraday cage to minimize external interference. The DAQ system is connected to the computer, facilitating data acquisition and analysis. (C) A 5-hour-long signal was recorded from the fungi on the 14th day, taken from a 30-day dataset of a small plate. (D) Graph illustrating the heights and widths of the mycelia's spontaneous action potentials. (E) Fungal spiking frequency and sampling time. (F and G) Histogram distribution of action potential peaks and widths. In (F), the histogram shows action potential peaks with the observed data fitted using a skew-normal distribution (green bars), and the black dashed lines represent a fit to the distributed data. The mean (μ) of the peaks is 126.487 μ V with an SD (σ) of 70.371 μ V. (G) The peak widths were also fitted using a skew-normal distribution; the mean (μ) is 1.106 s with an SD (σ) of 1.104 s. (H) Weekly analysis of fungal signal for spiking peak and frequency. The bars represent the mean action potential and spiking frequency values. Error bars represent the SD of the measurements. Each weekly dataset consists of a 48-hour period, with a sample size of $n = 1,728,000$ data points collected at a frequency of 10 Hz from a 30-day period, totaling 25,920,000 samples. S-W1 to S-W4 denote data from the small plate from the first to the fourth week, respectively, and B-W1 to B-W4 similarly represent data from the large plate from the first to the fourth week.

thresholding, peak identification, and peak analysis. We reported eight signal characteristics, including the analysis of spontaneous action potentials over time; probability density distribution for signal peaks, heights, and widths; and the relationships between height and width, height and time, width and time, and spiking frequency (peaks s^{-1}).

We applied the Savitzky-Golay filter (61) to a set of digital data points for the purpose of smoothing. We chose this filter because it is particularly effective at reducing noise while preserving the key

features of the signal, making it highly suitable for a variety of time series data applications. The filter operates by fitting a polynomial of a specified order to the data points within a certain window size. For our application, we used a third-order polynomial ($k = 3$) and a commonly used window size of 11 points ($n = 11$); see Eq. 2.

$$V_{\text{filtered},i} = \sum_{j=-\frac{n-1}{2}}^{\frac{n-1}{2}} c_j \cdot V_{i+j} \quad (2)$$

where $V_{\text{filtered},i}$ is the smoothed voltage value at point i , V_{i+j} is the original voltage data points, and c_j is the filter coefficient.

To identify signal peaks in fungal datasets, for each data point V_i in the fungal signal array $V_{\text{fungi}} = [V_1, V_2, \dots, V_n]$, we applied a condition: If V_i is greater than its immediate neighbors ($V_i > V_{i-1}$ and $V_i > V_{i+1}$), then V_i is considered a peak. We also set a prominence level to be compared with a predefined threshold.

For determining peak height and width, we extracted the voltage peak and the defined region using Eq. 3, adopted from (62), followed by estimating the height using Eq. 4. The first step involved calculating the evaluation height, after which the function identified the left and right boundaries of the peak height. The peak width was then estimated as the horizontal distance between these boundaries, providing a precise measurement of the peak's width in the voltage data. This approach offers valuable insights into the signal's characteristics by accurately determining the peak dimensions.

$$V_p(t) = V_{\text{raw}}(t) - B(t) - P \quad t \in [t_1, t_2] \quad (3)$$

$$h_{\text{eval}} = h_p(t) - P \cdot h_r \quad (4)$$

where $V_p(t)$ is the peak voltage, $V_{\text{raw}}(t)$ is the fungal raw voltage signal, $B(t)$ is the mean baseline voltage, P is the prominence, h_{eval} is the evaluation height, $h_p(t)$ is the peak height, h_r is the relative height, and $[t_1, t_2]$ is the peak region.

We identified the baseline voltage, $B(t)$, and net baseline voltage changes $\Delta B(t)$ of the recorded signal from both mycelium and control plates as approximately less than 2 μV . We implemented the peak detection model in Python, as shown in the flowchart in fig. S6. For a detailed description of the experiment design, please refer to the Fungal signal analysis method and Statistical analysis sections.

Figure 2C presents a 5-hour fungal signal, specifically highlighting the 14th day of recording from a small plate (Fig. 1A). Our results show the existence of multiple bands of signal widths (τ_{native}), such as 1.5, 2, and 2.5 s (see Fig. 2D). Furthermore, we observed that the spiking frequency (ξ_{native}) can reach up to 36 peaks min^{-1} , with a mean of 11 peaks min^{-1} (refer to Fig. 2E). The V_{native} had an average value of $\sim 194 \mu\text{V}$, with a maximum positive peak of 1140 μV and a negative spike of $-216 \mu\text{V}$ (Fig. 2F). The mean spike height was 60 μV , with a range of up to 1000 μV , as reported in Fig. 2G and fig. S7A. The mean τ_{native} was 1.1 s, and the $\tau_{\text{native}}^{\text{max}}$ was ~ 10 s, as shown in Fig. 2G and fig. S7 (C and D). In addition, we analyzed complete fungal data for both plates. We selected 48 hours of data from each week over a 30-day period. We discussed the detailed results in the Small and large petri dish mycelium scaffold weekly data analysis section in the Supplementary Methods. The corresponding figures for the small plate datasets are figs. S8 to S11, and the figures for the large plate datasets are figs. S12 to S15. The complete analyzed results show that the mean baseline potential for both plates reached $V_{\text{native}} \sim 135 \mu\text{V}$ with maximum peaks of $V_{\text{native}} \sim 1868 \mu\text{V}$ and minimum peaks of $V_{\text{native}} \sim 35 \mu\text{V}$ (Fig. 2H). Similarly, the mean spiking frequency varied around $\xi_{\text{native}} \sim 0.12 \text{ spikes s}^{-1}$, with a maximum of $\xi_{\text{native}} \sim 0.6 \text{ spikes s}^{-1}$ over the course of the 30-day recordings (Fig. 2E and figs. S8 to S15).

In our study, we used the light-sensing abilities of *Pleurotus* mycelia to alter the trajectory of our robots. We conducted tests using four types of light (UV, blue, red, and white) and measured the resulting voltage spikes. From our results, we found that fungi were more

sensitive to UV light stimulation, so we ran several tests with variations in intensity, duration, and height. We also tested for other light responses (blue, red, and white) at optimized UV exposure parameters. We discussed the detailed experimental procedure and setup in fig. S16 (A and B) and in the UV light stimulation setup section and the Blue, red, and white (BRW) light stimulation setup section in the Supplementary Methods (63). For our control data, we measured the voltage over time from agar medium without mycelium growth and repeated all of the experiments at least seven times.

We report the UV stimulation data from two different plates. In Fig. 3A, we report data from the first plate with variations in UV intensity from $0.1 \text{ W cm}^{-2} < \Gamma < 1 \text{ W cm}^{-2}$ at a UV source height of 12 cm. We analyzed V_{light} and τ_{light} at full width at half maximum (FWHM). We observed a consistent increase in action potential amplitude, ranging from $V_{\text{light}} = 25 \pm 4 \mu\text{V}$ at 0.1 W cm^{-2} to $V_{\text{light}} = 281 \pm 14 \mu\text{V}$ at 1 W cm^{-2} with a constant width of $1.3 \pm 0.1 \text{ s}$ (see fig. S16, C and D). In contrast, UV stimulation of the agar plate alone did not show any substantial spiking activity (refer to fig. S16E). For the second mycelium plate, we observed even larger peaks ranging between $V_{\text{light}} = 208 \pm 72 \mu\text{V}$ and $V_{\text{light}} = 18,569 \pm 1772 \mu\text{V}$ (refer to fig. S16F). We also conducted variable exposure height tests by adjusting the gap between the UV source and the plate in UV tests, ranging from 12 to 20 cm, and varied the exposure time of UV light from 2 to 12 s. We have included all analyzed data in Table 1 and in fig. S17 (A to E).

We found that, at longer wavelengths beyond UV, our mycelium scaffold only responded to blue light stimulation, with V_{light} potentials reaching $83 \pm 11 \mu\text{V}$ at an illumination distance of 12 cm and an exposure time of 2 s. We did not, however, observe any spontaneous response in the mycelium when exposed to red and white light. We did not see any red and white light response in agar plates (see fig. S17, F and G).

Mycelium-directed CPG control model

We categorized the mycelium signals into two types: positive electrical potentials (positive V_{native} ; Fig. 3Bi) and negative electrical potentials (negative V_{native} ; Fig. 3Bii) as depicted in Fig. 3B. From these analog spikes, we identified four distinct signals. These four analog signals were then converted into four digital control inputs as depicted in Fig. 3B (iii and vi).

The first type of signal input consisted of spontaneous action potential spiking trains converted to constant digital control signals, transforming V_{native} height information into constant or binary (0, 1) digital signals, as shown in Fig. 3Biii. The second type of signal input involved spontaneous action potential spiking trains being converted into variable digital control signals, translating V_{native} height information into variable pulse width modulation (PWM) signals, normalized between 0 and 255, also illustrated in Fig. 3Biv. The third type of control input was a UV-stimulated signal with artificially generated high-frequency digital signals. We used the V value as a threshold; if V_{light} was more than the mean V_{native} , then we generated artificial high-frequency digital signals (Fig. 3Bv). The fourth type of control input was a UV light-stimulated central pattern generation (CPG) as a digital control signal, using only V_{light} height information and translating it into constant PWM signals (Fig. 3Bvi). In addition, we incorporated τ_{light} for all applied signals at 80% of the detected peak height.

To allow these mycelia to operate the mechatronic system of the robot, we developed algorithms to test control scenarios that read

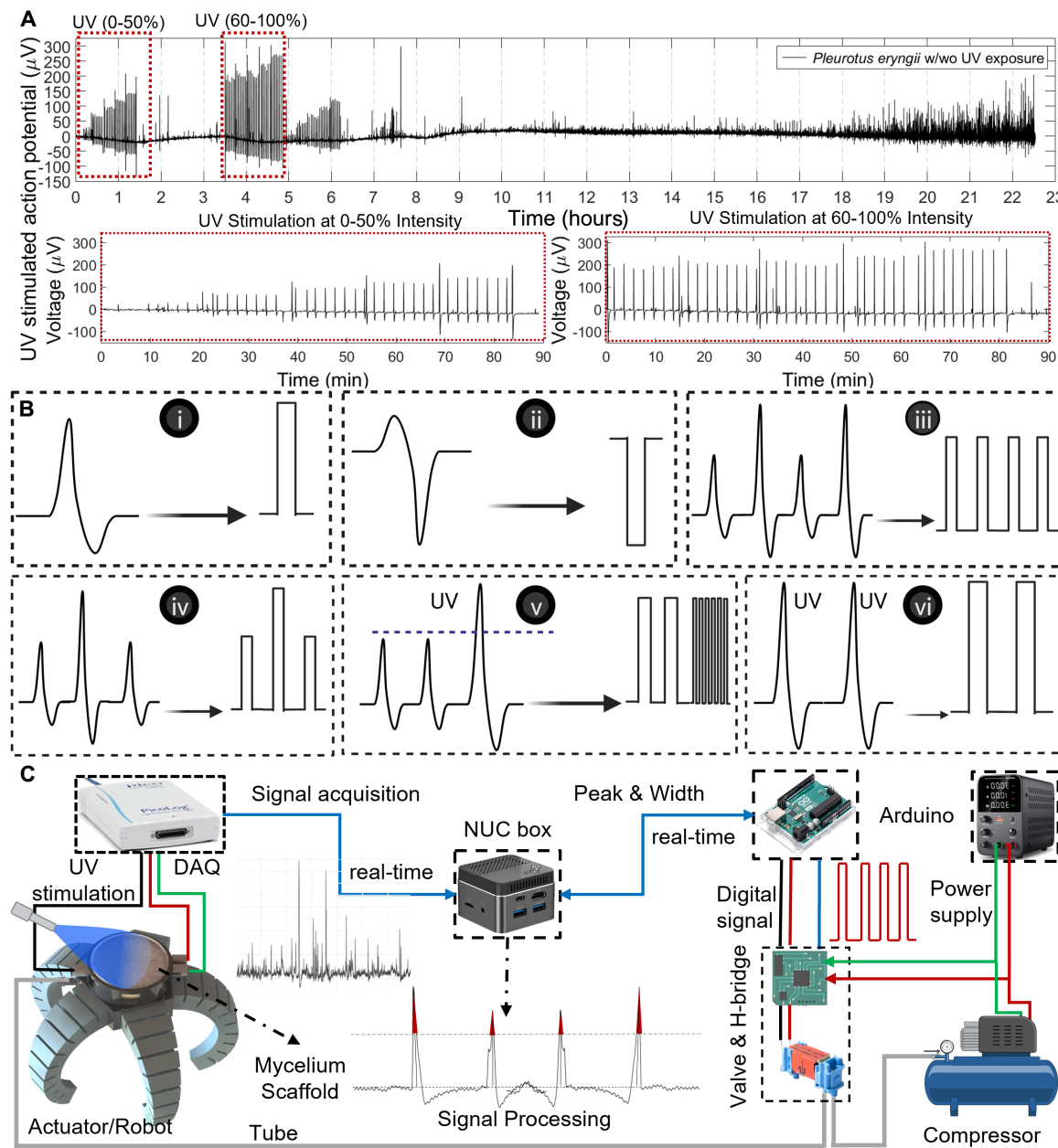


Fig. 3. Light stimulation and control signals. (A) A 24-hour UV-stimulated electrical recording for mycelia at variable UV intensities. (B) Illustration of mycelium signal to digital control signals: (i) Positive action potential translated to digital control signal. (ii) Negative action potential to digital control signal. (iii) Action potential pulses used for CPG-like control with constant PWM. (iv) Action potential pulses used for CPG-like control with variable PWM. (v) UV-stimulated feedback-controlled artificial signals. (vi) UV light-stimulated action potential pulses translated to digital control signals. (C) Block diagram illustrating the control architecture of mycelium-directed control in both robots.

Types of tests/measurements	Variable height		Variable exposure time	
	14 cm	20 cm	2 s	12 s
V_{light}	$736 \pm 48 \mu\text{V}$	$306 \pm 12 \mu\text{V}$	$237 \pm 41 \mu\text{V}$	$499 \pm 52 \mu\text{V}$
τ_{light}	$2 \pm 0.1 \text{ s}$	$2 \pm 0.1 \text{ s}$	$1.4 \pm 0.4 \text{ s}$	$5 \pm 0.1 \text{ s}$

the mycelium signal spiking trains at 30-s intervals and translate them into CPG-like digital control signals (Fig. 3C). The algorithms consisted of three major data processing steps, all performed in real time: signal acquisition, signal computation, and control signal generation and transmission to the robots. We discussed the detailed control process through a flowchart, which is available in fig. S18A, the Mycelium-directed robot control method section, and movie S1. We reported the mycelium signal sampled every 30 s and performed real-time calculations for 10 min to detect peak existence and measure peak width (see fig. S18B). We then implemented the CPG to control both tethered and untethered biohybrid robots.

Robot control strategies and demonstrations

We used these signal processing techniques to translate the action potentials emitted by the hyphae to control either valves or motors in the robots that we built. We used valves for a pneumatically actuated legged robot and motors for an untethered and wheeled hard robot. We demonstrated both robots in three control scenarios.

Native, V_{native} electrophysiological control

For V_{native} control, which we anticipate could be useful in substantially varying environmental conditions, we used both constant and variable PWM signals. We transmitted the width and height information of the spontaneous fungal signal to the MCU. The peak height and width were mapped to a digital signal. By translating the fungal peak information into digital output pins using PWM mode, we represented the signal as either high (1) or low (0). We incorporated fungal width information using delay functions between each high and low state. For soft robots, we used only one digital output pin to activate and deactivate the valve; for the motor encoder system, we used two digital output pins; and for the wheeled robot, we used a total of eight digital output pins with combinations of high and low signals with a constant PWM.

Because the V_{native} peaks of the mycelium signal are not constant, we incorporated both the height and width information. We extracted the peak and width information from the mycelium signal and normalized the height value to the highest PWM value. This approach allowed for automatic adjustment of duty cycles and effective voltage (as described in Eq. 5)

$$V_{\text{eff}} = V_s \frac{\tau_o}{\tau_p} \quad (5)$$

V_{eff} is the effective voltage, V_s is the maximum supply voltage, τ_o is on time, and τ_p is the period.

Light-stimulated, V_{light} electrophysiological, high-frequency control

Before starting a demonstration, we first exposed the mycelial scaffold to UV light. We then estimated the height ratio between V_{light} and V_{native} . From our experiments, the height ratios were 3 to 10 times larger than the spontaneous signal. We then set a threshold value of typically $\sim 3 V_{\text{native}}$, such that whenever the UV light exposure caused the mycelium signal to surpass it, we generated a high-frequency signal from the MCU at 100% duty cycle without using the fungal peak height and width properties.

Light-stimulated, V_{light} electrophysiological, native control

We followed a similar approach to the V_{native} -based control signals, but, in this case, we used only UV-stimulated spike width and height information. We exposed the mycelium plate to UV light for 1 s at a

20-s interval to generate a light-stimulated spiking pattern. We then followed the robot with the UV source, periodically exposed the mycelia to it, and incorporated each UV-stimulated spike into the digital signal for control.

Tethered legged soft robot

We designed a starfish-like tethered robot with five soft-legged actuators (L_1 , L_2 , L_3 , L_4 , and L_5) in an isosceles trapezoidal shape, featuring interconnected chambers and a strain-limiting layer for bending motion. We connected these actuators to a pentagonal central base using an internal channel and a barbed tube connector, enabling actuation from a single pressure source, as depicted in fig. S19A. For movement, the robot uses an asymmetric friction method within its feet [$F_s > (F_{r1}, F_{r2}, F_{r3}, F_{r4})$] to locomote efficiently on flat surfaces (64). It involves use of four low-friction rigid materials for the feet (F_{r1} , F_{r2} , F_{r3} , and F_{r4}) and one high-friction elastomer foot (F_s), depicted in fig. S19B.

To facilitate real-time control of locomotion using V_{native} and V_{light} signals from fungi, we mounted a mycelial scaffold atop the robot. Ensuring seamless integration between the robot's body and the scaffold is crucial for movement success, especially in isolating external EMI and mechanical interferences and simplifying scaffold replacement. For this integration, we adopted plug and socket joints, with the plug part designed on the base and the socket part on the scaffold, both in a pentagonal shape. To mitigate mechanical noise, we used soft pads and elastomers, and, for electrical noise insulation, we implemented a copper mesh layer to ground the electrodes to the base. Moreover, we ensured a tight fit between the plug and socket components to eliminate any relative movement between the robot body and the scaffold during locomotion, as illustrated in fig. S19C.

We also used a pressure sensor to gauge the robotic actuation output, aligning it with the mycelium input signal. It allowed us to verify the actuator's response time and the width of the fungal signal, ensuring precise synchronization between the robot's movements and the mycelium inputs.

For fabrication, we 3D-printed the legged robot using both soft and rigid materials, constructing it as a monolithic structure through a multimaterial design approach. The robot's elastomer offers viscoelasticity and a low elastic modulus, providing inherent compliance, vibration damping, and noise reduction. We include more design and fabrication details in fig. S19 (A to E), the Soft legged robot design and fabrication section, and the Soft legged robot 3D printing fabrication procedure section in the Supplementary Methods. For the wiring, we connected mycelium electrodes to an ADC and used the microcontroller to issue commands to the valve. We discussed the complete circuit and wiring details in fig. S20, the Soft legged robot electronics section in the Supplementary Methods, and the Pressure sensor integrated soft robot for signal I/O mapping setup section.

We began demonstrating the soft robot on a wooden table with mycelium-directed V_{native} and its corresponding digital output as a change in actuation pressure, control scenario 1. First, we conducted a 10-min test of the robot without attaching the mycelium scaffold to the robot's body but instead placing it inside the Faraday cage (refer to fig. S21A and movie S2). During this test, the robot was only connected to air sources, although the rest of the electronics, scaffold, valve, sensor, and MCU were kept inside the Faraday cage. We then demonstrated the robot with the mycelium scaffold

attached to it for 20 min [reported input and output (I/O) data in Fig. 4, A and B, and movie S3].

For control scenario 2, we activated Arduino signals at a frequency of 1 Hz whenever the UV-stimulated voltage height was more than 100 μV . We conducted again tests on the robot both with and without the mycelium scaffold attached to its body. Initially, we tested the robot without the mycelium scaffold for 4 min (see fig. S21B and movie S4), followed by a test with the scaffold attached for 7 min (refer to Fig. 4, C and D, and movie S5). Last, we tested control scenario 3, shown in fig. S21 (C and D) and movie S6. All three mycelium-directed control scenarios were able to drive the soft robot. In addition, mycelium input and robot output signal verification showed an alignment between the spiking signals and the corresponding robot pressure under all three tested conditions, with minor computational delays.

Untethered wheeled robot

We designed an untethered wheeled robot for fast movement, incorporating a four-wheel drive system, as shown in fig. S22A. Our multilevel design seamlessly integrates mechanical components, electronics, and power supplies. At the base level, we installed a four-wheel drive mechanism comprising four dc motors, brackets, and an ac-dc power supply, illustrated in fig. S22 (B and C). We equipped each motor with wheels and synchronized the circuit to ensure uniform direction of motor rotation. On the second level, we placed the mini-PC, MCU, and motor control circuit, centralizing the electronic components.

To enable mycelium-directed control using V_{native} and V_{light} signals, we mounted a mycelium scaffold, electrode connectors, and a PicoLog DAQ system on the top level, as seen in fig. S22D. We

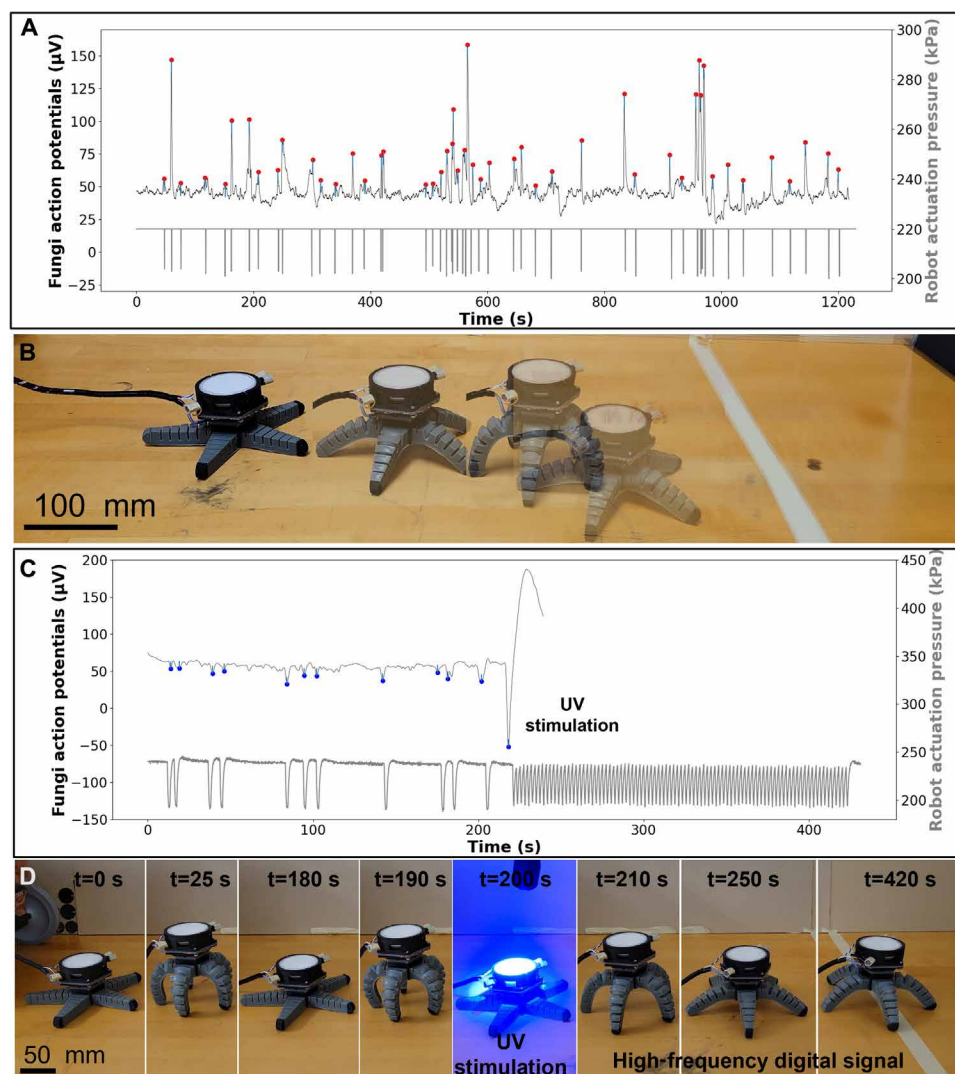


Fig. 4. Demonstrations of the mycelium-directed tethered soft robot in different control scenarios. (A) Graph illustrating fungal signals (V_{native}) over a 20-min period and their corresponding digital signals used to control the starfish-like soft robot. (B) Soft robot walking on the table with an integrated mycelium scaffold, using signals reported in (A). (C) Graph displaying the I/O signals of V_{light} , which are feedback-controlled artificial signals. (D) Robot motion is controlled by the I/O signals of V_{light} , which are feedback-controlled artificial signals in (C). The robot initially moves using V_{native} , and, after UV exposure, it accelerates, moving faster because of a high-frequency artificial digital signal.

tackled mechanical and EMI disturbances, such as ground vibration noise, external perturbations, mini-PC fan noise, and electromagnetic noise from the power supply and wiring, with various strategies. We incorporated a vibration isolation system (VIS) between the second and third levels using vibration-damping materials, shock-absorbing sponges, and rubber-coated wheels to reduce mechanical noise. In addition, we placed a sand bed and sponge pads on the third level to dampen vibrations from the robot's movement, securing the plate and electrodes in sand on all sides except the top and stabilizing the PicoLog against internal movements. To counteract electrical disturbances, we equipped all levels with Faraday cages and ensured proper soldering of ground connections with copper mesh.

We fabricated the wheeled robot through 3D printing and traditional assembly methods, including nuts, bolts, screws, and glue. For detailed information on the design and fabrication process, refer to the Supplementary Materials and the Untethered wheeled robot design and fabrication section.

We connected the motor wires to the motor driver PCB, powered the mini-PC with ac, and supplied the motors with dc from an ac-dc power source. We have documented the complete wiring diagrams, circuit fabrication, and electronics for the wheeled robot in fig. S23A and the Untethered wheeled robot electronics section in the Supplementary Methods. Before implementing full robot control, we first tested a single motor with an encoder on a motor testbed setup (depicted in fig. S23B and the Encoder-integrated dc motor for signal I/O mapping setup section) to ensure that the fungal input signals synchronized with motor rotation, applying the same testing approach used with the legged robot actuators.

We reported signal motor control results in fig. S24 (A to D), movies S7 to S9, and the Motor encoder mapping results section in the Supplementary Methods. We first tested for 10 min where the mycelium scaffolds, electronics, and MCU were placed in the Faraday cage and transmitted the signal directly to a motor outside of the environment. We observed mycelium signals exhibiting positive and negative V_{native} , and then, we mapped the mycelium input signals to encoder output in the form of motor revolution counts.

We then conducted the wheeled robot demonstrations. First, we performed a demonstration indoors using control scenario 1, where we allowed the robot to drive for 15 min using mycelium action potentials ranging between $95 < V_{\text{native}} < 130 \mu\text{V}$ (Fig. 5, A and B, and movie S10). We then tested control

scenario 2, where UV excitation caused the robot to move away from the light source. The mycelium data along with the time stamp of robot movement and the corresponding video can be found in Fig. 5 (C and D) and movie S11. Last, we conducted control scenario 3, moving the UV light source along the V_{light} -controlled robot. During these experiments, we shone UV light onto the mycelium six times for 3 min, resulting in recorded V_{light} peaks of $\sim 350 \mu\text{V}$ with a width of $\sim 4 \text{ s}$ at 80% FWHM. The corresponding data can be seen in fig. S24E and movie S12.

CONCLUSION

We have successfully demonstrated a biohybrid robot controlled by bioelectric signals from fungal mycelium. We confirmed that the spontaneous and evoked electrical signals originated from living fungi by comparing recordings from agar plates without fungi with agar plates before and after the mycelium growth reached our extracellular electrodes (46, 51). Our focus was to adapt these electrical signals for biological sensing and robotic commands.

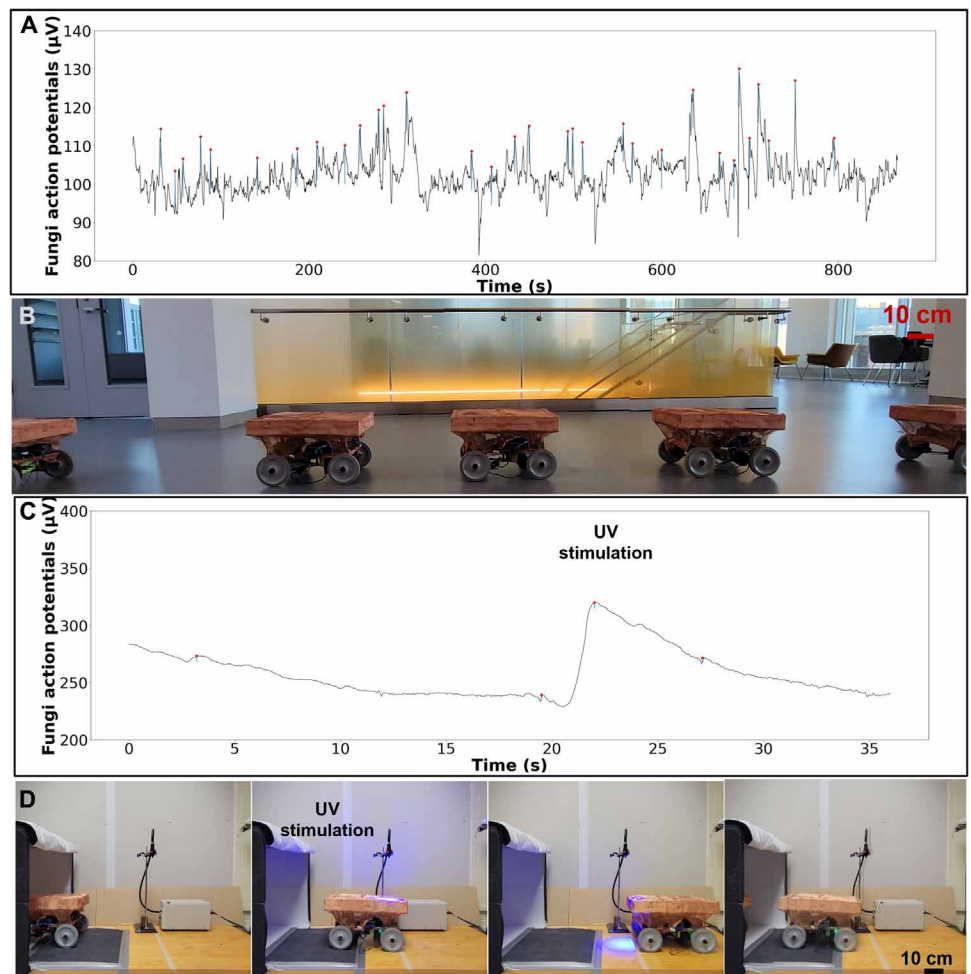


Fig. 5. Mycelium-directed untethered wheeled robot demonstration in different control scenarios. (A) Graph representing the mycelium-directed output signal with constant PWM. (B) The robot demonstration corresponding to the graph in (A), moving in a building using V_{native} . (C) Graph depicting the UV-stimulated spikes as feedback signal with artificial control. (D) Robot demonstration corresponding to the graph in (C); robot came out of the box, and, after UV exposure, it went back using a high-frequency artificial digital signal.

Our innovations include a 3D-printed mycelial scaffold for stable long-term recordings, UV and blue light stimulation response in mycelia, and a control architecture inspired by central pattern generators observed in the animal kingdom (65, 66). We used these advances to cause movement in legged and wheeled robots over long durations while capturing dynamic environmental changes as feedback.

Using fungi for developing biohybrid robots brings several advantages over other approaches, such as more facile and low-cost culture protocols and low risk of contamination while interfacing with engineered systems. The mycelia have action potential–like activity and environmental sensing abilities (39) that persist for months, demonstrating the potential for real-world application, perhaps in agriculture or security.

Adapting electrophysiological mycelium signaling to biohybrid robotics presents several challenges that need to be addressed. Some of these challenges include the plasticity of fungal signals, with gradual weakening observed over time, and the difficulty of capturing low-amplitude signals ($<50\ \mu\text{V}$) at high sampling rates because of insufficient resolution. Another challenge is the 30-s data sampling interval that introduces a lag during V_{light} control because of fungal spiking frequencies. Choosing different sliding window configurations should reduce this lag. Further, and quite obviously, living systems die. Addressing these challenges calls for enhanced high-precision electronics for signal amplification, as well as techniques for regeneration and regrowth of the mycelia.

In the UV experiment, we tested both mycelia and their control. The experiments showed that UV-stimulated signals in the mycelia ranged from 600 to 17,000 μV , whereas those in agar-stimulated controls hovered around 10 to 20 μV . In conclusion, although some activity was observed in the controls, it was quite small compared with that of the mycelia, where signals were 60- to 1000-fold larger. To more accurately quantify the effects of UV stimulation, however, further validation through biochemistry and genomics is needed to isolate our measurements from potential heat effects.

Last, this emerging field of fungal biohybrids warrants increased cooperation, standardization, and effort. Fungal electrophysiology has been studied by a few researchers, such as Slayman *et al.* (45) and Olsson and Hansson (46) through intracellular electrophysiology, and Adamatzky and Gandia (50, 51, 57) have focused on EEP. We have introduced the measurement of spiking action potentials from filamentous mycelia to control mobile robots. As the field grows, standards for comparison (signaling, hardware, wetware, organisms) will be important to measure progress.

MATERIALS AND METHODS

Fungal culture protocols

We cultured the fungi in sterilized conditions using a biosafety cabinet (BSC). To achieve a contamination-free and pure fungiculture, maintaining a sterilized condition is crucial. The fungal culture is a multistep process [see fig. S1 (steps 1 to 7)].

Medium preparation and sterilization

In our fungal model, we used potato dextrose agar (PDA). For medium preparation, we used a recipe of 3.6% (w/v) PDA powder and mixed in deionized water in an Erlenmeyer flask. We covered the flask with aluminum foil to prevent it from spilling. After preparing the liquid medium, we then mixed it using a magnetic stirrer for

15 min. We sterilized the medium in an autoclave for 45 min using 30-min sterilization and 15-min cooling cycles at 34.47 kPa and 120°C. We also used autoclave tape to ensure that the medium was completely sterilized (fig. S1, steps 1 to 4).

Medium transfer

After the autoclaving cycle finished, we let the flask cool for 20 to 30 min until we could comfortably hold it. We then poured the medium into polystyrene circular-shaped large [150 mm (diameter, D) by 15 mm (height, H)]– and small [60 mm (D) by 15 mm (H)]–size petri dishes under the BSC. We regulated the amount of the medium in the petri dishes using a weighing scale so that the fungi could easily grow over the electrodes. For example, for small petri dishes, we used 14.5 to 15 g, and, for large petri dishes, we used 50 to 54 g of agar. Furthermore, we waited at least 4 hours for gelation of the medium in petri dishes (fig. S1, step 5).

Fungal inoculation

After gelling medium in petri dishes, we started inoculating the fungi. We first purchased a *P. eryngii* (king oyster) mushroom kit from Amazon.com (root mushroom farm) and then grew it until it produced a fruiting body. We inoculated our first culture from the fruiting body. We began the process for fungal inoculation by spraying disinfectant in the BSC and turning on the filter for 15 min. We then sprayed 70% (v/v) ethanol and wiped the BSC again. Then, we put medium plates in the BSC as well as a live fruiting body. We sterilized a scalpel using 100% ethanol and directly exposed it to fire from a burner. We then cut small pieces from the inner side of the fruiting body to ensure a clean surface, transferred them into a medium plate, and repeated the process for multiple petri dishes. Last, we closed the petri dish lids and wrapped them with parafilm to prevent any further contamination (fig. S1, step 6).

Fungal incubation

We stored multiple plates in an incubator at room temperature. We waited for 3 weeks and 5 weeks for the mycelia to grow fully in the small and large petri dishes, respectively (fig. S1, step 7).

Subcultures

We used a clean culture as a master plate and regularly inoculated several plates for subcultures following the same procedure (steps 1 to 7). We continued to transfer the fungus to freshly prepared medium every month to keep it alive and vigorous for future studies.

3D-printed mycelium scaffold

Scaffold hardware design

To provide a substrate for mycelia and an electrical interface with our mechatronic system, we designed and 3D-printed a mycelium culture plate using a Carbon M1 printer and polyurethane materials (RPU, Carbon Inc.; Fig. 1, B and C). These plates feature three electrode inputs (E_1 , E_2 , and E_{GND} ; MN4022D10S#, Spes Medica, Italy; see Fig. 1B). The scaffold consisted of a petri dish containing agar medium, freshly inoculated mycelia, three electrodes (E_1 , E_2 , and E_{GND}), connectors to hold the electrodes, an antivibration electrometric pad, and a casing to secure the petri dish. The casing replicated a petri dish and was precisely designed to position the electrodes. For electrode attachment, we used a Luer lock mechanism to enable easy attachment and detachment of plug and socket connectors. The electrodes were integrated into the socket connector and secured with dental cement to prevent internal movement. Two electrodes (E_1 and E_2) were positioned in parallel, 10 mm from the sides and 10 and 11 mm from the base of the petri dishes, respectively. The E_{GND} electrode was placed at 180° and 1 mm from the base of the petri dish (as shown in Fig. 1C).

Fabrication

The scaffold fabrication involved three major steps: initially, creating a computer-aided design 3D model using SOLIDWORKS software (SolidWorks Corp., Dassault Systèmes); subsequently, converting the 3D models into .stl file format before printing; and lastly, engaging in 3D printing and postprocessing. In our setup, we divided the casing in half for easy integration and 3D-printed all its components using a Carbon M1 printer (Carbon Inc.) with rigid polyurethane (RPU 70, 1.7-GPa tensile modulus, 30% elongation at break).

Casing and electrode integration

To prepare for measuring fungal action potential signals, we integrated all electrodes and mycelium plates with the casing. We placed a 3D-printed elastomeric antivibration pad with a thickness of 1 mm on the base of the scaffold before integrating the petri dish. We attached the petri dish to the casing using Teets cold cure dental cement (Co-ORAL-ITE Dental Mfg. Co.) and waited for over 30 min until they were fully bonded. Then, we made small holes for the electrodes using a 1-mm metal rod heated with a burner flame and passed it through the plug holders' holes to ensure that they were concentric. We inserted the electrodes into the socket connectors and locked them with dental cement. After the electrodes were fully integrated into the connectors, we inserted them into the plug connectors and locked them using a Luer lock mechanism. Last, we added paper tape around the connectors and electrode wires to ensure that there was no movement (refer to Fig. 1, B and C).

Fungal signal recording setup

In our experimental design, we used twisted subdermal needle electrodes made of stainless steel, lead wire from Cu/Sn with polyvinyl chloride (PVC) coating, and a connector with Cu/Zn with PVC jacket. Specifically, we used electrodes of 220-mm length and 0.4-mm diameter (Spes Medica, Italy, intraoperative monitoring neurodiagnostic electrodes). To record signals, we used a PicoLog 24-bit ADC high-resolution data acquisition system (DAQ) (Pico Technology, 16 S/s, four digital I/O channel maximum of ± 2500 mV and minimum of ± 39 mV, and 16 single-ended voltage/8 differential voltage inputs). We connected the DAQ to PicoLog software and used three electrodes: two for differential input and one for ground input with ± 39 mV channel at a 10 S/s (<500 -nV resolution) setting.

To protect against unexpected vibrations and other interference such as electromagnetic impact, we built a large Faraday cage and isolated the recording system. We constructed a large Faraday cage (1 m by 1 m by 1.5 m) using a heavy metal block. The Faraday cage was covered by copper mesh from all sides and wrapped with black cloth to block out light. To prevent high-amplitude mechanical noise, we used buckets filled with sand at the four corners of the Faraday cage. To ensure long periods of experiments, we minimized the opening of the Faraday cage (refer to Fig. 2B and fig. S4, A and B).

Fungal signal analysis method

We stored the large datasets of fungal signals in CSV format, representing action potential values in microvolts versus the number of samples, for analysis. We classified any fungal signal below $5 \mu\text{V}$ as noise and excluded it from further analysis. For algorithm development, we used Python (version 3.9.13) with the SciPy signal library. Our focus included specific time periods: a single 14th day for a 5-hour dataset from the small plate and 48-hour datasets collected every 7 days from both small and large plates. We sampled the data

at 30-s intervals, a rate sufficient to observe at least one or two peaks. After sampling, we applied the Savitzky-Golay filter to remove electronic noise and smooth any signals below $5 \mu\text{V}$. We also defined the baseline potential and prominence (P), setting $P = 10 \mu\text{V}$ for all analyses of fungal signals, addressing both positive and negative spikes. The data were then imported into our developed code, and we analyzed eight signal characteristics, as discussed in the section Signal processing and analysis.

To identify the peaks, we used the `find_peaks` and `peak_widths` functions, using a predefined prominence. The `find_peaks` function estimated the signal peak and height between depolarization and repolarization from the baseline, as the `peak_widths` function calculated the width, representing the time between depolarization and repolarization at 80% of the spike height. Subsequently, we created arrays for time, peak, height, and width over the given duration as shown through a flow chart in fig. S6. On the basis of these data, we generated histograms for signal peak, height, and width over the 48-hour period. In addition, we counted the number of peaks and normalized it by the sampling time. We also plotted the action potentials versus time, height versus width, height versus time, and width versus time. The results are presented in Fig. 2 (C to G) and figs. S7 to S15. Refer to the Small and large petri dish mycelium scaffold weekly data analysis section in the Supplementary Methods for further discussion of the results.

UV light stimulation setup

For UV sensing, we prepared the same setup as used and discussed in the Fungal signal recording setup section. Once the mycelium plate and recording setup were completed, we proceeded to set up the UV light source. We used an OmniCure versatile UV mercury lamp (OmniCure S1500 Spot UV curing system, 435-nm Excelitas Technologies Corp.) equipped with a long flexible optical fiber cable and a collimator (fig. S16A).

The OmniCure lamp was placed outside the Faraday cage, and the optical fiber cable with collimator was clamped onto a variable height stand using a gripper. We ensured that the UV lens was set up to irradiate the scaffold surface perpendicularly. In addition, we used a UV shield for our safety and protection. As a control experiment, we used an agar (PDA) plate without any mycelium inoculation. During the UV sensing experiment, we performed several tests to examine the effects of variable exposure height, variable exposure intensity, and variable exposure time and repeated each set of experiments at least seven times.

Variable intensity exposure

We conducted an experiment to study the effect of UV radiation on fungi by increasing the UV power intensity from 0.1 to 1 W cm^{-2} . Throughout the experiment, we maintained a constant height of the UV source at 12 cm and irradiated the fungi with UV light for 2 s. We waited for 2 min between each illumination event to determine the optimal duration of illumination and to minimize the influence of heat emitted by the light source on the fungus. To ensure precise intensity adjustments, we carefully adjusted the position of the light source.

Variable height exposure

We conducted variable height tests at an intensity of 0.1 W cm^{-2} , following similar steps as the variable intensity test. However, in this case, we varied the distance between the mycelium plate and collimator of the light source. The height was adjusted from 12 to 20 cm

with 2-cm increments. The purpose of using a low intensity was to minimize any potential damage to the fungus during the experiment.

Variable time exposure

We conducted a time duration test to assess the effect of increasing durations of irradiation on fungi. We started with an initial duration of 2 s and gradually increased it up to 12 s. In addition, we tested different time intervals between illuminations. On the basis of the results of these experiments, we determined that an interval of 2 min between each irradiation event provided optimal conditions. Furthermore, throughout the experiments, we maintained a consistent height of 12 cm and intensity of 0.1 W cm^{-2} .

Mycelium-directed robot control method

To enable real-time control, we designed an on-demand control algorithm that performs all signal processing in real time. The algorithm consists of three main substeps: real-time data acquisition, real-time data computation, and real-time control signal generation, as illustrated in Fig. 3C, fig. S18A, and movie S1. This process involves continuously reading the mycelium signals and saving the data every 30 s. The algorithm then analyzes the first 30 s of data, extracting peak width and height information to generate control signals and reprogram the MCU in situ. We created three program files that were sequentially executed from the command prompt: the data acquisition file, followed by the data computation file, and lastly the robot control file. The detailed algorithm flow chart can be found in fig. S18A.

For real-time data acquisition, we used a PicoLog DAQ, along with a custom-built Python program (version 3.9.13) that enabled us to sample the mycelium signal and process it. In Python, we used the Pico SDK library to configure and access the PicoLog device.

The voltage range and conversion time (sampling rate) were set to $\pm 39 \text{ mV}$ and 100 ms (10 S s^{-1}), respectively, to accurately record the mycelium signal. We applied a conversion formula provided by the PicoLog datasheet, as shown in Eq. 6, to interpret the recorded signal

$$V = \frac{\text{ADC Value}_{\text{raw}}}{\text{ADC Value}_{\text{max}}} \times V_{\text{max}} \quad (6)$$

Here, $\text{ADC Value}_{\text{raw}}$ refers to the raw data obtained from the fungi, $\text{ADC Value}_{\text{max}}$ represents the maximum ADC count, and V_{max} denotes the voltage range of the dataset. Because our objective involved not only reading the data but also processing it for control purposes, we saved fungal data points in a text file every 30 s at a sampling rate of 10 S/s , resulting in a total of 300 data points per file. Depending on the experimental requirements, we saved text files for different durations in real time from 10 to 60 min.

For real-time computation, we began analyzing the signal properties, specifically peak width and height. To ensure stability in the membrane potential, we discarded the initial 30-s data. We implemented Python code (version 3.9.13) using the SciPy signal library, as discussed in the Fungal signal analysis method section. By defining the baseline potential (baseline) and setting a prominence threshold of $10 \text{ } \mu\text{V}$, we detected fungal spikes above this threshold, including both positive and negative spikes. To smoothen the signal below $5 \text{ } \mu\text{V}$, we applied the Savitzky-Golay filter. The `find_peaks` and `peak_widths` commands were used to estimate spike height and width, respectively. We reported a 10-min signal with detection of fungal signal in fig. S18B and in situ process in movie S1.

For real-time control signal generation, we provided fungal height and width information from the 30-s text file to Arduino for robot control, continuously updating this information every 30 s using the saved text file. We also developed robot control in Python and interfaced Python with Arduino. We used the pyFirmata library (version 1.1.0), which enabled access to the Arduino microcontroller and allowed for real-time reprogramming with the fungal information.

Soft legged robot design and fabrication

We fabricated a starfish robot as a monolithic structure through a hybrid approach, using polyurethane chemistry-based soft and rigid resins to create the soft monolithic robot. Our process involved three steps. First, we designed 3D models of the robot's components using SOLIDWORKS software and converted them into .stl files for printing. Next, we printed individual components, such as actuators and the base body. Then, we assembled these components at the uncured stage and subjected them to thermal baking. This process, because of the shared chemistry of the soft and rigid materials, allowed for polymerization between the heterogeneous materials, resulting in a single body. This means that we can produce a monolithic robotic structure with a hybrid material approach, achieving complex soft robotic structures—in this case, a monolithic starfish-like soft robot.

The dimensions of the actuator are a length of 62.7 mm , a base width of 25.5 mm , a top width of 10 mm , and a height of 16 mm . The central body with a side length of $l_1 = 30 \text{ mm}$ and a height of $h_1 = 25.5 \text{ mm}$; the plug scaffold connector measures $l_2 = 30 \text{ mm}$ by $h_2 = 15 \text{ mm}$, and the socket scaffold connector measures $l_3 = 30 \text{ mm}$ by $h_3 = 10 \text{ mm}$. For additional details on the mycelial scaffold setup, refer to the 3D-printed mycelium scaffold section.

We used a high-resolution digital light synthesis printer (Carbon M1, Carbon Inc.) to print the components. Last, we assembled the printed parts by using thermal baking and fastening techniques such as glue, screws, and nuts. We built the robot with a multimaterial approach, soft and rigid. We used UV-curable silicone elastomer (SIL30, tensile modulus of 3 MPa , elongation at break of 350% , Carbon Inc.) for soft components such as the leg actuators, scaffold plug connector, soft pad, and soft foot (F_s). Conversely, we used RPU 70 (tensile modulus of 1.7 GPa , elongation at break of 30% , Carbon Inc.) for rigid components, including the central base, barbed tube connector, rigid feet (F_{r1} , F_{r2} , F_{r3} , and F_{r4}), and scaffold socket connector. The multimaterial and multistep 3D-printing method is discussed in the Soft legged robot 3D printing fabrication procedure section in the Supplementary Methods.

Pressure sensor integrated soft robot for signal I/O mapping setup

In the soft robot setup, we used the same electronic components and circuits as described in the Soft legged robot electronics section in the Supplementary Methods. In addition, we incorporated an analog pressure sensor (SSCDANN150PGAA5, 1034.21 kPa , vented gauge, 0.5 to 4.5 V , 8-DIP) from Honeywell Sensing and Productivity Solutions (digikey.com). The sensor, with three pins (V_{supply} , V_{out} , and ground), was connected between the robot's inlet and valve outlet using a T-shaped barbed connector (refer to fig. S20). To read the data from the sensor, we used an additional Arduino. The V_{out} pin was connected to an analog read pin (A0), V_{supply} to 5 V , and ground to the ground pin. We captured the data in the serial monitor at the

same sampling rate as the mycelium signal (10 Hz) and saved the pressure data in an Excel file.

Untethered wheeled robot design and fabrication

We constructed the untethered wheeled robot in the same manner as the tethered soft robot except we used a fused deposition modeling (FDM) printer for most of the components and assembled them with screws and nuts. We used an Ultimaker S5, an extrusion-based FDM printer from Ultimaker USA Inc., to print the robot base, battery support structure (first and second floor), fungi, and datalogger tray (third floor). These components were printed using polylactic acid filaments in black and transparent colors sourced from Maker-Bot Industries LLC, with a tensile modulus of 3.3 GPa and an elongation at break of 7.8%. For the motor brackets, wheel-motor connectors, and VIS support structure, we used urethane methacrylate (UMA 90), a resin with a tensile modulus of 1.7 GPa and an elongation at break of 30%, sourced from Carbon Inc., and printed them using the Carbon M1 printer.

We initiated the fabrication process by 3D-printing the motor brackets, wheel connectors, and the robot base. For this purpose, we used four shock-resistant thermoplastic rubber (TPE) tread hard polypropylene core wheels sourced from McMaster-Carr, with a diameter of 12.7 cm and a width of 2.2 cm. In addition, we selected four dc motors for motion, which we securely fixed into brackets and then connected to the wheels using 3D-printed connectors. We fastened them in place using screws and nuts. Subsequently, we attached an X-shaped frame to the brackets both to prevent tilting and to house the battery pack.

Upon finalizing the wheel-motor drive chassis, we firmly affixed it to a rectangular base measuring 320 cm by 230 cm. After that, we connected the VIS module and affixed antivibration foam rubber mats sourced from XCEL via Amazon.com to the robot base. These mats were composed of Neoprene foam with pressure-sensitive adhesive, measuring 152.5 mm (length, L) by 152.5 mm (width, W) by 6.25 mm (H). The VIS module was composed of four 3D-printed fixtures and four shock-absorbing, vibration-damping disk-shaped pads purchased from Sonvera Pads via Amazon.com. An attachment was used to establish the connection between the VIS module and the tray.

Next, we securely positioned the minicomputer, motor control circuit, and MCU on a sponge mat embedded base. Subsequently, we proceeded to 3D print the tray using an FDM printer with dimensions of 410 cm (L) by 300 cm (W) by 5 cm (H). To create compartments, we included a partition within the tray. The connectors of the VIS module were then attached to the four corners of the tray and tightly secured using antivibration pads, using a peg and hole joint. We divided the partition into sections, dedicating one section to PicoLog wiring and the other section to the 3D-printed mycelial scaffold. We show the complete robot schematic and assembled prototype in fig. S22 (A to D).

Encoder-integrated dc motor for signal I/O mapping setup

For the wheeled robot test, we used a motor encoder setup. We used a micro metal geared brushed motor (6 V, 31 RPM, 100 mA, 12 kg-cm, 1.6 A) and a quadrature encoder with a hall effect sensor and magnets (12 CPR, 2.7 to 18 V) sourced from pololu.com. The motor was fixed on a 3D-printed stand. The motor control circuit is the same as described in the wheeled robot control section. Furthermore, we used a single motor using the same configuration but added an extra Arduino to read the motor's output signals from the encoder. The encoder had four pins: two for V_{supply} and GND and two output

pins (A and B) for digital reading. We connected the V_{supply} and ground pins to the Arduino's 5 V and GND pins, respectively, and the A and B pins to digital input pins. We read the data in the serial monitor, saved it in an Excel file, and then plotted the mycelium-directed input signals and encoder output signals together at the same sampling rate. The complete circuit diagram is shown in fig. S23B.

Statistical analysis

We calculated the mean values and SDs (\pm SD) for all electrical measurements. For example, in our weekly analysis, we used 48-hour datasets, each containing 1,728,000 samples, from a total pool of 25,920,000 samples. We conducted skew-normal distribution analysis on these datasets, estimating both the mean and the SD of the detected peak probability distributions. Similarly, in the light-stimulation experiments, we repeated the light stimulation at least seven times ($n = 7$) under identical conditions and then calculated the mean and SD of all detected peak values.

Supplementary Materials

The PDF file includes:

Methods

Figs. S1 to S24

Other Supplementary Material for this manuscript includes the following:

Movies S1 to S12

MDAR Reproducibility Checklist

REFERENCES AND NOTES

1. V. E. Abraira, D. D. Ginty, The sensory neurons of touch. *Neuron* **79**, 618–639 (2013).
2. G. Corniani, H. P. Saal, Tactile innervation densities across the whole body. *J. Neurophysiol.* **124**, 1229–1240 (2020).
3. Y. Morimoto, H. Onoe, S. Takeuchi, Biohybrid robot powered by an antagonistic pair of skeletal muscle tissues. *Sci. Robot.* **3**, eaat4440 (2018).
4. Y. Tanaka, S.-I. Funano, Y. Noguchi, Y. Yalikun, N. Kamamichi, A valve powered by earthworm muscle with both electrical and 100% chemical control. *Sci. Rep.* **9**, 8042 (2019).
5. M. Crepaldi, C. Mohan, E. Garofalo, A. Adamatzky, K. Szaciłowski, A. Chiolerio, Experimental demonstration of in-memory computing in a ferrofluid system. *Adv. Mater.* **35**, 2211406 (2023).
6. B. de Lacy Costello, A. Adamatzky, N. M. Ratcliffe, C. Melhuish, Experimental reaction-diffusion chemical processors for robot path planning. *J. Intel. Robot. Syst.* **37**, 233–249 (2003).
7. H. Yokoi, A. Adamatzky, B. de Lacy Costello, C. Melhuish, Excitable chemical medium controller for a robotic hand: Closed-loop experiments. *Int. J. Bifurcation Chaos* **14**, 3347–3354 (2004).
8. M.-A. Tsompanas, C. Fullerton, A. Adamatzky, Belousov-Zhabotinsky liquid marbles in robot control. *Sens. Actuators B* **295**, 194–203 (2019).
9. A. Adamatzky, B. de Lacy Costello, C. Melhuish, N. Ratcliffe, Experimental implementation of mobile robot taxis with onboard Belousov-Zhabotinsky chemical medium. *Mater. Sci. Eng. C* **24**, 541–548 (2004).
10. A. Chiolerio, M. B. Quadrelli, Smart fluid systems: The advent of autonomous liquid robotics. *Adv. Sci.* **4**, 1700036 (2017).
11. L. Ricotti, B. Trimmer, A. W. Feinberg, R. Raman, K. K. Parker, R. Bashir, M. Sitti, S. Martel, P. Dario, A. Menciassi, Biohybrid actuators for robotics: A review of devices actuated by living cells. *Sci. Robot.* **2**, eaaq0495 (2017).
12. R. W. Carlsen, M. Sitti, Bio-hybrid cell-based actuators for microsystems. *Small* **10**, 3831–3851 (2014).
13. L. Gao, M. U. Akhtar, F. Yang, S. Ahmad, J. He, Q. Lian, W. Cheng, J. Zhang, D. Li, Recent progress in engineering functional biohybrid robots actuated by living cells. *Acta Biomater.* **121**, 29–40 (2021).
14. C. Cvetkovic, R. Raman, V. Chan, B. J. Williams, M. Tolish, P. Bajaj, M. S. Sakar, H. H. Asada, M. T. A. Saif, R. Bashir, Three-dimensionally printed biological machines powered by skeletal muscle. *Proc. Natl. Acad. Sci. U.S.A.* **111**, 10125–10130 (2014).
15. R. Raman, C. Cvetkovic, S. G. M. Uzel, R. J. Platt, P. Sengupta, R. D. Kamm, R. Bashir, Optogenetic skeletal muscle-powered adaptive biological machines. *Proc. Natl. Acad. Sci. U.S.A.* **113**, 3497–3502 (2016).
16. S.-J. Park, M. Gazzola, K. S. Park, S. Park, V. Di Santo, E. L. Blevins, J. U. Lind, P. H. Campbell, S. Dauth, A. K. Capulli, F. S. Pasqualini, S. Ahn, A. Cho, H. Yuan, B. M. Maoz, R. Vijaykumar,

- J.-W. Choi, K. Deisseroth, G. V. Lauder, L. Mahadevan, K. K. Parker, Phototactic guidance of a tissue-engineered soft-robotic ray. *Science* **353**, 158–162 (2016).
17. Y. Kim, Y. Yang, X. Zhang, Z. Li, A. Vázquez-Guardado, I. Park, J. Wang, A. I. Efimov, Z. Dou, Y. Wang, J. Park, H. Luan, X. Ni, Y. S. Kim, J. Baek, J. J. Park, Z. Xie, H. Zhao, M. Gazzola, J. A. Rogers, R. Bashir, Remote control of muscle-driven miniature robots with battery-free wireless optoelectronics. *Sci. Robot.* **8**, eadd1053 (2023).
 18. O. Aydin, X. Zhang, S. Nuethong, G. J. Pagan-Diaz, R. Bashir, M. T. A. Saif, Neuromuscular actuation of biohybrid motile bots. *Proc. Natl. Acad. Sci. U.S.A.* **116**, 19841–19847 (2019).
 19. D. Blackiston, E. Lederer, S. Kriegman, J. Bongard, M. Levin, A cellular platform for the development of synthetic living machines. *Sci. Robot.* **6**, eabf1571 (2021).
 20. S. Kriegman, D. Blackiston, M. Levin, J. Bongard, Kinematic self-replication in reconfigurable organisms. *Proc. Natl. Acad. Sci. U.S.A.* **118**, e2112672118 (2021).
 21. S. Kriegman, D. Blackiston, M. Levin, J. Bongard, A scalable pipeline for designing reconfigurable organisms. *Proc. Natl. Acad. Sci. U.S.A.* **117**, 1853–1859 (2020).
 22. H. Herr, R. G. Dennis, A swimming robot actuated by living muscle tissue. *J. Neuroeng. Rehabil.* **1**, 6 (2004).
 23. J. C. Nawroth, H. Lee, A. W. Feinberg, C. M. Ripplinger, M. L. McCain, A. Grosberg, J. O. Dabiri, K. K. Parker, A tissue-engineered jellyfish with biomimetic propulsion. *Nat. Biotechnol.* **30**, 792–797 (2012).
 24. V. A. Webster, K. J. Chapin, E. L. Hawley, J. M. Patel, O. Akkus, H. J. Chiel, R. D. Quinn, “*Aplysia californica* as a novel source of material for biohybrid robots and organic machines” in *Biomimetic and Biohybrid Systems: 5th International Conference, Living Machines 2016, Edinburgh, UK, July 19–22, 2016. Proceedings*, N. F. Lepora, A. Mura, M. Mangan, P. F. M. J. Verschure, M. Desmulliez, T. J. Prescott, Eds., vol. 9793 of *Lecture Notes in Artificial Intelligence* (Springer, 2016), pp. 365–374.
 25. Y. Tanaka, Y. Noguchi, Y. Yalikun, N. Kamamichi, Earthworm muscle driven bio-micropump. *Sens. Actuators B* **242**, 1186–1192 (2017).
 26. M. Kawai, M. Nie, H. Oda, Y. Morimoto, S. Takeuchi, Living skin on a robot. *Matter* **5**, 2190–2208 (2022).
 27. K. Warwick, S. J. Nasuto, V. M. Becerra, B. J. Whalley, “Experiments with an in-vitro robot brain” in *Computing With Instinct: Rediscovering Artificial Intelligence*, Y. Cao, Ed., vol. 5897 of *Lecture Notes in Computer Science* (Springer, 2011), pp. 1–15.
 28. A. Verma, M. Verma, A. Singh, “Animal tissue culture principles and applications”, in *Animal Biotechnology*, A. S. Verma, A. Singh, Eds. (Elsevier, ed. 2, 2020), pp. 269–293.
 29. S. J. Park, S.-H. Park, S. Cho, D.-M. Kim, Y. Lee, S. Y. Ko, Y. Hong, H. E. Choy, J.-J. Min, J.-O. Park, S. Park, New paradigm for tumor theranostic methodology using bacteria-based microrobot. *Sci. Rep.* **3**, 3394 (2013).
 30. N. Koumakis, A. Lepore, C. Maggii, R. Di Leonardo, Targeted delivery of colloids by swimming bacteria. *Nat. Commun.* **4**, 2588 (2013).
 31. Y. Hiratsuka, M. Miyata, T. Tada, T. Q. Uyeda, A microrotary motor powered by bacteria. *Proc. Natl. Acad. Sci. U.S.A.* **103**, 13618–13623 (2006).
 32. D. Parker, Y. Daguerre, G. Duflil, D. Mantione, E. Solano, E. Cloutet, G. Hadzioannou, T. Näsholm, M. Berggren, E. Pavlopoulou, E. Stavrinidou, Biohybrid plants with electronic roots via in vivo polymerization of conjugated oligomers. *Mater. Horizons* **8**, 3295–3305 (2021).
 33. F. Meder, I. Must, A. Sadeghi, A. Mondini, C. Filippeschi, L. Beccai, V. Mattoli, P. Pinguet, B. Mazzolai, Energy conversion at the cuticle of living plants. *Adv. Funct. Mater.* **28**, 1806689 (2018).
 34. W. Li, N. Matsuhisa, Z. Liu, M. Wang, Y. Luo, P. Cai, G. Chen, F. Zhang, C. Li, Z. Liu, Z. Lv, W. Zhang, X. Chen, An on-demand plant-based actuator created using conformable electrodes. *Nat. Electron.* **4**, 134–142 (2021).
 35. R. Sachse, A. Westemeier, M. Mylo, J. Nadassdi, M. Bischoff, T. Speck, S. Poppinga, Snapping mechanics of the Venus flytrap (*Dionaea muscipula*). *Proc. Natl. Acad. Sci. U.S.A.* **117**, 16035–16042 (2020).
 36. O. Vincent, C. Weisskopf, S. Poppinga, T. Masselter, T. Speck, M. Joyeux, C. Quilliet, P. Marmottant, Ultra-fast underwater suction traps. *Proc. Biol. Sci.* **278**, 2909–2914 (2011).
 37. S. Tsuda, S. Artmann, K.-P. Zauner, “The phi-bot: A robot controlled by a slime mould” in *Artificial Life Models in Hardware*, A. Adamatzky, M. Komosinski, Eds. (Springer, 2009), pp. 213–232.
 38. J. Heitman, B. J. Howlett, P. W. Crous, E. H. Stukenbrock, T. Y. James, N. A. R. Gow, *The Fungal Kingdom* (John Wiley & Sons, 2020).
 39. Y.-S. Bahn, C. Xue, A. Idnurm, J. C. Rutherford, J. Heitman, M. E. Cardenas, Sensing the environment: Lessons from fungi. *Nat. Rev. Microbiol.* **5**, 57–69 (2007).
 40. N. Magan, Fungi in extreme environments. *The Mycota* **4**, 85–103 (2007).
 41. T. Ohnuki, F. Sakamoto, N. Kozai, K. Nanba, H. Neda, Y. Sasaki, T. Niizato, N. Watanabe, T. Kozaki, Role of filamentous fungi in migration of radioactive cesium in the Fukushima forest soil environment. *Environ. Sci.: Processes Impacts* **21**, 1164–1173 (2019).
 42. C. Gostinčar, P. Zalar, N. Gunde-Cimerman, No need for speed: Slow development of fungi in extreme environments. *Fungal Biol. Rev.* **39**, 1–14 (2022).
 43. M. Parniske, Arbuscular mycorrhiza: The mother of plant root endosymbioses. *Nat. Rev. Microbiol.* **6**, 763–775 (2008).
 44. M. L. Smith, J. N. Bruhn, J. B. Anderson, The fungus *Armillaria bulbosa* is among the largest and oldest living organisms. *Nature* **356**, 428–431 (1992).
 45. C. L. Slayman, W. S. Long, D. Gradmann, “Action potentials” in *Neurospora crassa*, a mycelial fungus. *Biochim. Biophys. Acta Biomembranes* **426**, 732–744 (1976).
 46. S. Olsson, B. Hansson, Action potential-like activity found in fungal mycelia is sensitive to stimulation. *Naturwissenschaften* **82**, 30–31 (1995).
 47. Z. Yu, R. Fischer, Light sensing and responses in fungi. *Nat. Rev. Microbiol.* **17**, 25–36 (2019).
 48. A. Idnurm, J. Heitman, Photosensing fungi: Phytochrome in the spotlight. *Curr. Biol.* **15**, R829–R832 (2005).
 49. J. C. Dunlap, J. J. Loros, How fungi keep time: Circadian system in *Neurospora* and other fungi. *Curr. Opin. Microbiol.* **9**, 579–587 (2006).
 50. A. Adamatzky, A. Gandia, On electrical spiking of *Ganoderma resinaceum*. *Biophys. Rev. Lett.* **16**, 133–141 (2021).
 51. A. Adamatzky, On spiking behaviour of oyster fungi *Pleurotus djamar*. *Sci. Rep.* **8**, 7873 (2018).
 52. R. R. Lew, Mapping fungal ion channel locations. *Fungal Genet. Biol.* **24**, 69–76 (1998).
 53. B. P. Bean, The action potential in mammalian central neurons. *Nat. Rev. Neurosci.* **8**, 451–465 (2007).
 54. A. Nikolaïdou, N. Phillips, M.-A. Tsompanas, A. Adamatzky, Responsive fungal insoles for pressure detection. *Sci. Rep.* **13**, 4595 (2023).
 55. A. Adamatzky, A. Gandia, A. Chiolerio, Towards fungal sensing skin. *Fungal Biol. Biotechnol.* **8**, 1–7 (2021).
 56. S. Gantenbein, E. Colucci, J. Käch, E. Trachsel, F. B. Coulter, P. A. Rühls, K. Masania, A. R. Studart, Three-dimensional printing of mycelium hydrogels into living complex materials. *Nat. Mater.* **22**, 128–134 (2023).
 57. A. Adamatzky, Language of fungi derived from their electrical spiking activity. *R. Soc. Open Sci.* **9**, 211926 (2022).
 58. J. Cao, M. Sun, M. Yu, Y. Xu, J. Xie, H. Zhang, J. Chen, T. Xu, X. Qian, S. Sun, Transcriptome analysis reveals the function of a G-protein α subunit gene in the growth and development of *Pleurotus eryngii*. *J. Fungi* **9**, 69 (2023).
 59. S. L. Hooper, J. Schmidt, “Electrophysiological recording techniques” in *Neurobiology of Motor Control: Fundamental Concepts and New Directions*, S. L. Hooper, A. Büschges, Eds. (Wiley, 2017), pp. 7–53.
 60. L. Breckenridge, R. J. Wilson, P. Connolly, A. S. Curtis, J. A. Dow, S. E. Blackshaw, C. D. Wilkinson, Advantages of using microfabricated extracellular electrodes for in vitro neuronal recording. *J. Neurosci. Res.* **42**, 266–276 (1995).
 61. A. Savitzky, M. J. Golay, Smoothing and differentiation of data by simplified least squares procedures. *Anal. Chem.* **36**, 1627–1639 (1964).
 62. P. Du, W. A. Kibbe, S. M. Lin, Improved peak detection in mass spectrum by incorporating continuous wavelet transform-based pattern matching. *Bioinformatics* **22**, 2059–2065 (2006).
 63. I. Vilinsky, K. L. Hibbard, B. R. Johnson, D. L. Deitcher, Probing synaptic transmission and behavior in *Drosophila* with optogenetics: A laboratory exercise. *J. Undergrad. Neurosci. Educ.* **16**, A289 (2018).
 64. R. F. Shepherd, F. Ilievski, W. Choi, S. A. Morin, A. A. Stokes, A. D. Mazzeo, X. Chen, M. Wang, G. M. Whitesides, Multigait soft robot. *Proc. Natl. Acad. Sci. U.S.A.* **108**, 20400–20403 (2011).
 65. H. X. Ryu, A. D. Kuo, An optimality principle for locomotor central pattern generators. *Sci. Rep.* **11**, 13140 (2021).
 66. E. Marder, D. Bucher, Central pattern generators and the control of rhythmic movements. *Curr. Biol.* **11**, R986–R996 (2001).

Acknowledgments: We gratefully acknowledge the use of facilities and instrumentation supported by the NSF through the Cornell University Materials Research Science and Engineering Center (DMR-1719875). A.K.M. extends gratitude to the Engineering Living Materials Institute (ELMI) at Cornell University for providing postdoctoral fellowship funding. We also appreciate the valuable contributions of Y. Zhang, a master’s student, and A. Samardzija, an undergraduate student, both from the Department of Mechanical and Aerospace Engineering at Cornell University, to this project. Special thanks are extended to B. Land, emeritus senior lecturer in the Department of Electrical and Computer Engineering at Cornell University, and S. Olsson from Fujian Agriculture and Forestry University, Fuzhou, China, for insightful guidance and assistance. **Funding:** This work was supported by the National Science Foundation (NSF) CROPPS Science and Technology Center under award no. DBI-2019674; United States Department of Agriculture (USDA), National Institute of Food and Agriculture (NIFA) under contract no. 2021-67021-33843; and National Science Foundation Signal in Soil under contract no. IOS-2034351. **Author contributions:** Conceptualization: A.K.M. and R.F.S. Methodology: A.K.M., J.K., H.B., B.R.J., K.T.H., and R.F.S. Investigation: A.K.M., J.K., and H.B. Visualization: A.K.M., J.K., H.B., B.R.J., K.T.H., and R.F.S. Funding acquisition: R.F.S. Project administration: A.K.M. and R.F.S. Supervision: R.F.S. Writing—original draft: A.K.M. and R.F.S. Writing—review and editing: A.K.M., J.K., H.B., B.R.J., K.T.H., and R.F.S. **Competing interests:** The authors declare that they have no competing interests. **Data and materials availability:** All data needed to support the conclusions of this manuscript are included in the main text or Supplementary Materials. The reported raw datasets, as well as the code for data analysis and robot control, can be accessed at Zenodo (<https://doi.org/10.5281/zenodo.12812074>). We also included data analysis and robot control codes on GitHub (<https://github.com/Alchemist77/fungi-data-analysis> and <https://github.com/Alchemist77/fungi-robot-control>).

Submitted 11 September 2023
Accepted 30 July 2024
Published 28 August 2024
10.1126/scirobotics.adk8019